Journal of Rock Mechanics and Geotechnical Engineering 18 (2026) 3804–3818

Contents lists available at ScienceDirect

Journal of Rock Mechanics and Geotechnical Engineering

journal homepage: www.jrmge.cn

Full Length Article

Thermoelastic and viscosity-temperature effects on fracture propagation in deep reservoirs: A numerical study

Yunpeng Wang [a,b], Ming Chen [a,b,*], Tiankui Guo [a,b], Jiwei Wang [c], Bo Zhang [a,b,d], Zhanqing Qu [a,b]

[a] State Key Laboratory of Deep Oil and Gas, China University of Petroleum (East China), Qingdao, 266580, China
[b] School of Petroleum Engineering, China University of Petroleum (East China), Qingdao, 266580, China
[c] School of Safety Engineering, China University of Mining and Technology (Xuzhou), Xuzhou, 221116, China
[d] Laoshan Laboratory, Qingdao, 266100, China

ARTICLE INFO

Article history:
Received 30 March 2025
Received in revised form
13 July 2025
Accepted 31 July 2025
Available online 7 November 2025

Keywords:
Deep reservoir hydraulic fracturing
Fracture propagation
Thermal effects
Thermoelastic stress
Viscosity-temperature effect (VTE)
Proppant transport

ABSTRACT

In this study, the influences of the thermoelastic effect and fluid viscosity-temperature effect (VTE) on hydraulic fracture growth in deep reservoirs were investigated. A computational model that integrates the thermoporoelastic effect and VTE was developed on the basis of the displacement discontinuity method (DDM). The temperature distribution within fractures is determined using a first-order upwind scheme. Using this simulator, this study systematically evaluated the impacts of the poroelastic stress, thermoelastic stress, and VTE of the fracturing fluid on fracture propagation. Furthermore, the dominant controlling factors were identified in both the viscosity- and toughness-dominated regimes. The results show that (1) the thermoelastic stress exhibits behavior opposite to that of poroelastic stress, reducing the injection pressure and increasing the fracture width. (2) Under viscosity-dominated conditions, the influence of the VTE is more remarkable, whereas the thermoelastic effect on fracture propagation is relatively weak. Under toughness-dominated conditions, the influence of the thermoelastic effect on fracture propagation remains relatively weak, and the VTE can essentially be disregarded. (3) When proppant transport is considered, for small proppant particles, the transport distance increases from 88 m to 100 m when the VTE is considered because the VTE increases the fracture length. For large proppant particles, owing to the decrease in viscosity with increasing temperature, the proppant transport distance is significantly reduced from 86 m to 70 m. These results indicate that reasonably selecting the proppant size and paying more attention to the VTE of the fracturing fluid in deep reservoir fracturing are crucial.

1. Introduction

Owing to increasing global energy demand, deep and ultradeep oil and gas resources have emerged as strategic alternatives to conventional reservoirs. However, these reservoirs are typically characterized by high temperatures (120 °C–220 °C), high pressures (70–150 MPa), strong heterogeneity, and extremely low permeabilities (<0.1 mD), which pose significant challenges for development.

Hydraulic fracturing has become the core means of economically developing deep oil, gas, and geothermal reservoirs (Guo et al., 2022). The high temperature of the reservoir rock affects fracture propagation via thermal stress induced by the cool fluid injected during hydraulic fracturing and the viscosity-temperature effect (VTE) of the fluid in the fractures (i.e. the change in viscosity with temperature). This constitutes a strong thermohydromechanical coupling process, which is challenging to model and simulate efficiently. As a result, the mechanism of fracture propagation in deep reservoirs remains ambiguous, and the influence of thermal effects on fracture propagation is highly uncertain, thereby significantly restricting the engineering design of deep reservoir fracturing.

* Corresponding author. State Key Laboratory of Deep Oil and Gas, China University of Petroleum (East China), Qingdao, 266580, China.
E-mail address: chenmingfrac@163.com (M. Chen).

Peer review under responsibility of Institute of Rock and Soil Mechanics, Chinese Academy of Sciences.

https://doi.org/10.1016/j.jrmge.2025.07.027

The process of propagating hydraulic fractures in deep reservoirs is influenced by both poroelastic and thermal effects. The poroelastic effect arises from fluid leakage from fractures into reservoir pores, which increases reservoir pressure and thereby induces poroelastic stress (Dontsov, 2021). The thermal effects consist of two parts: the thermoelastic effect and the VTE of the fluid. The thermoelastic effect refers to the cooling and shrinkage of the surrounding rock due to the significant temperature difference when cold fluid is injected, thereby affecting the local stress distribution (An et al., 2025). The VTE of the fluid refers to the change in fluid viscosity with fluid temperature, which occurs because there is a large temperature difference from the near-wellbore region to the fracture front. In the field of hydraulic fracturing, most field-scale fracturing studies (Chen et al., 2020, 2022a, 2022b, 2024; Tan et al., 2020, 2023; Wang et al., 2023, 2024b; Xia et al., 2024) have not considered poroelastic and thermoelastic effects. Because the focus of this paper is on the analysis of thermal effects, a detailed analysis of poroelastic stress can be found in Dontsov (2021) and Sabah et al. (2025).

Extensive research has been conducted on the thermoelastic effect. Wang et al. (2024a) used the continuum-discontinuum element method to investigate thermomechanical coupling and reported that the thermoelastic effect can significantly increase the fracture width and reduce the breakdown pressure. The authors also elucidated the primary factors influencing fracture propagation in geothermal reservoirs. Lin et al. (2024) used the two-dimensional (2D) displacement discontinuity method (DDM) to further incorporate the thermoelastic effect and conducted simulations of multifracture propagation in high-temperature shale gas reservoirs. Both studies concluded that the thermal effect indicated the fracture width and reduced the formation breakdown pressure.

To explore the VTE of a fluid, Tang et al. (2016) conducted fracture propagation simulations using a three-dimensional (3D) DDM and reported that accounting for the VTE increased the fracture length and accelerated proppant settling. However, because the thermoelastic stress was not considered in their study, determining whether the thermoelastic stress or the VTE has a greater impact on fracture propagation is not feasible. Liu et al. (2025) simulated proppant transport within fractures in geothermal reservoirs using a 3D DDM and reported more remarkable proppant settling after the VTE was incorporated. However, because fracture propagation was not considered in their study, their conclusions may be somewhat limited. Additionally, because an increase in temperature reduces fluid viscosity, fracture tip breakdown may shift from a "viscosity-dominated" state to a "toughness-dominated" state (Detournay, 2004). During fracture propagation, the viscosity-dominated state refers to the consumption of a large amount of energy to overcome fluid flow resistance, whereas the toughness-dominated state refers to the consumption of a large amount of energy to break rock and form new fracture surfaces (Detournay, 2004). Current research on hydraulic fracture propagation in deep and ultradeep reservoirs is incomplete, and the fracture propagation mechanism influenced by thermal effects is not well understood.

In this work, we derived the displacement discontinuity expression for thermoelastic stress on the basis of the thermoelastic displacement potential. We also formulate the heat transfer equation for the fluid within hydraulic fractures and further incorporate the VTE of the fluid. We employed an efficient method (Dontsov, 2021) to calculate the poroelastic stress. We subsequently coupled these parts into our previously developed hydraulic fracture and proppant transport simulator (Wang et al., 2025a, 2025b). We then analyzed the effects of poroelastic stress, thermoelastic stress, and the VTE on the propagation of a single penny-shaped fracture.

The remainder of the paper is structured as follows: Section 2 presents the core mathematical models for heat transfer within fractures, the model of thermal effects and the poroelastic effects. Section 3 describes the numerical scheme employed. Section 4 provides the validation results for fracture propagation and heat transfer within hydraulic fractures. In Section 5, the influences of thermoelastic and poroelastic effects on fracture propagation are examined and contrasted. At the end of Section 5, the dominance of the thermoelastic effect versus the VTE in viscosity- and toughness-dominated regimes is discussed. In the discussion section (Section 6), our results are compared with those from other studies and appropriately extended the discussion to the area of proppant transport, with a brief analysis of the impact of thermoelastic and VTE effects on proppant transport and recommendations for field design.

2. Mathematical model

The following assumptions are made regarding complex fracture propagation, heat diffusion in reservoir rock, and heat transfer within hydraulic fractures:

(1) The rock in a deep reservoir is assumed to be a homogeneous, isotropic, and thermoporoelastic medium.
(2) The fracturing fluid within hydraulic fractures is incompressible and Newtonian, and the fracture and the fluid share a common front, i.e. no fluid lag exists (Gordeliy, 2011). The fluid leakage from the fracture to the formation pores is one-dimensional (1D) and is modeled using Carter's leak-off model (Carter, 1957).
(3) Considering the in situ stress conditions of deep reservoirs, hydraulic fractures are assumed to be planar and perpendicular to the horizontal plane.
(4) Due to the high flow rate of fluid in hydraulic fractures, heat transfer is dominated by convection; thus, heat diffusion is disregarded.
(5) The temperature diffusion in the formation rock, resulting from heat exchange between the fluid in the fracture and the rock matrix at the fracture walls, is 1D and perpendicular to the fracture plane (Fig. 1).

To be concise, avoid redundancy and highlight the core model of this paper, we omit the modules that describe rock deformation, fluid flow within fractures, the propagation criterion, and proppant transport. These modules can be found in our previously published papers (Wang et al., 2025a, 2025b).

2.1. Poroelasticity and calculation of the poroelastic stress

During the fracturing process, the fracturing fluid leaks into the reservoir pores through the fracture walls, resulting in an increase in pore pressure. This, in turn, induces rock deformation and stress changes, which are collectively referred to as poroelastic stress. Currently, some researchers (Zhang et al., 2023) have employed the finite element method to solve thermohydromechanical coupling problems. This method, which is a full-field discretization approach, incurs an excessively high computational cost for large-scale problems. To avoid this excessive computational burden, we use the efficient method proposed by Dontsov (2021) to compute the poroelastic stress. The calculation formula is

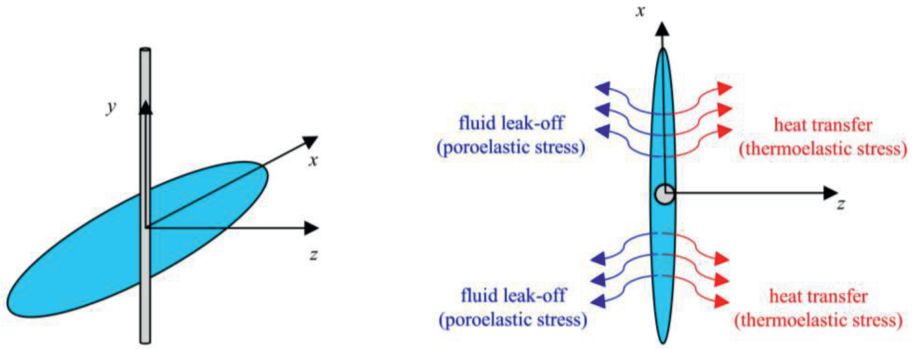

(a) Fracturing schematic (b) Top view of a hydraulic fracture

Fig. 1. Schematic diagrams of hydraulic fracturing, fluid leak-off, and heat exchange.

$$\left.\begin{aligned}\Delta\sigma_{ij}^{\mathrm{lo}} &= \frac{B}{4\pi}\frac{\partial}{\partial x_i \partial x_j}\int_S \frac{\Delta\overline{p}^{lo}}{\sqrt{(x-x')^2+(y-y')^2+z^2}}\mathrm{d}x'\mathrm{d}y' \\ B &= \alpha\frac{1-2\nu}{1-\nu}\end{aligned}\right\} \quad (1)$$

where α represents the Boit's coefficient; other details on poroelasticity can be found in Dontsov (2021).

2.2. Heat transfer within fractures

During the injection of cold fluid, a progressive temperature decrease develops within the fracture, establishing a distinct temperature gradient characterized between the wellbore and the fracture front. The model incorporates two fundamental assumptions: (1) the heating effects of the wellbore on the fluid are disregarded; and (2) the fluid is incompressible and Newtonian, and the heat conduction/diffusion between fluids is also disregarded. According to Liu et al. (2025), convective heat transfer is dominant in the temperature evolution process within hydraulic fractures, hence heat diffusion within the fluid phase is relatively negligible. Thus, heat transfer mechanisms within a fracture system involve two primary mechanisms: convective transport through fluid flow and conductive exchange at fracture-wall interfaces. The heat exchange between fracturing fluid within fractures and formations is controlled principally by the transient temperature gradient at the fracture wall. The governing thermal equation for this coupled system combines convective heat transport with wall conduction effects:

$$\frac{\partial(wT)}{\partial t}+\nabla\cdot\left[T\left(-\frac{w^3}{12\mu}\nabla pQ_{\mathrm{S}}(\overline{\phi})\right)\right]=2\frac{\lambda_{\mathrm{r}}}{c_{\mathrm{f}}\rho_{\mathrm{f}}}\frac{\partial T}{\partial n}\bigg|_{n=\pm w/2} \quad (2)$$

where c_{f} represents the specific heat capacity, λ_{r} represents the rock thermal conductivity, w denotes the fracture width, and ρ_{f} indicates the density of fluid.

Additionally, the variation in the temperature field also changes the viscosity of the fracturing fluid within the fractures, and an exponential model (Lin et al., 2024) is employed to describe this process.

$$\mu(T)=\mu_{\mathrm{ref}}\exp\left[-C_T\left(T-T_{\mathrm{ref}}\right)\right] \quad (3)$$

where T_{ref} represents the reference temperature, μ_{ref} denotes the fluid viscosity at T_{ref}, and C_{T} indicates the temperature sensitivity coefficient.

2.3. Heat diffusion within reservoir rock

During the relatively brief duration of hydraulic fracturing, which typically spans several hours, the fluid within the hydraulic fracture zone is subjected to gradual heating by the surrounding rock, while the formation rock experiences a corresponding cooling effect (see Fig. 2). Owing to the relatively small time scale of hydraulic fracturing, compared with the fracture size, the range of the temperature diffusion scale may be very small. Consequently, we simplify the heat diffusion within the formation rock as a 1D process oriented perpendicularly to the fracture plane. For the applicability of 1D models and the differences from 3D models, please refer to Appendix A. Additionally, the heat transfer induced by fluid leak-off is considered negligible. This 1D heat diffusion problem is governed by

$$\left.\begin{aligned}&\frac{\partial T}{\partial t}=D\frac{\partial^2 T}{\partial z^2}, D=\frac{\lambda_{\mathrm{r}}}{\rho_{\mathrm{r}}c_{\mathrm{r}}} \\ &\text{Initial condition}: T(z,0)=T_0, z>0 \\ &\text{Boundary condition}: T(0,t)=f(t), t\geq 0 \\ &\text{Boundary condition}: \lim_{z\to+\infty}T(z,t)=T_0\end{aligned}\right\} \quad (4)$$

where ρ_{r} represents the density of the rock, T_0 denotes the initial temperature of the formation, c_{r} indicates the specific heat capacity of the rock, and $f(t)$ represents the temperature variation at a certain location in the hydraulic fracture.

For fracture propagation simulations, the process typically employs a time-stepping scheme. Consequently, the boundary condition $f(t)$ in Eq. (4) is represented as a piecewise-constant function, where the temperature at a given location remains constant within each specific time step. Under these conditions, the exact solution of Eq. (4) is expressed as

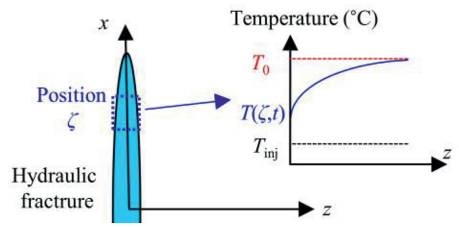

Fig. 2. Diagram of the temperature distribution in the outer normal direction of the fracture wall.

$$T(z,t) = T_0 + \sum_{k=1}^{n} \left\{ [f(t_k) - T_0] \left[\operatorname{erfc}\left(\frac{|z|}{\sqrt{4D(t-t_{k-1})}} \right) - \operatorname{erfc}\left(\frac{|z|}{\sqrt{4D(t-t_k)}} \right) \right] \right\} \tag{5}$$

where t denotes the current time, the subscripts $k-1$ and k represent the time step indices, and D represents the diffusion coefficient (Eq. (4)). By using Eq. (5), the temperature gradient at the fracture wall can be conveniently calculated.

2.4. Thermoelasticity and efficient calculation of the thermoelastic stress

According to thermoelasticity theory, rock displacement resulting from thermal expansion is irrotational (Goodier, 1937; Ghassemi et al., 2005). Consequently, the displacement component in each direction can be expressed as the derivative of the thermoelastic potential function Φ, that is, $\Phi_{,i}$. By substituting this equation into the stress equilibrium equation, a 3D Poisson's equation for the thermoelastic potential function Φ is derived. For this 3D Poisson equation, the application of the Green's function method facilitates the formulation of an expression for calculating the thermal stress as

$$\left.\begin{aligned} \sigma_{ij} &= \frac{Gm}{2\pi} \frac{\partial^2}{\partial x_i \partial x_j} \int_V \frac{\Delta T(x',y',z')\mathrm{d}x'\mathrm{d}y'\mathrm{d}z'}{\sqrt{(x-x')^2+(y-y')^2+(z-z')^2}} - 2Gm\Delta T\delta_{ij} \\ m &= \frac{1+\nu}{1-\nu}\alpha^{\mathrm{T}} \end{aligned}\right\} \tag{6}$$

where G represents the shear modulus, ν denotes the Poisson's ratio, ΔT indicates the change in temperature, and α^{T} represents the coefficient of linear thermal expansion. For the detailed derivation process, please refer to the literature (Goodier, 1937; Ghassemi et al., 2005). The integral is taken over the entire region of temperature diffusion, which is a 3D domain.

In Section 2.3, we use the 1D heat diffusion assumption to compute the heat exchange between the fluid and reservoir rock; here, we still use this assumption to compute the thermoelastic stress. By using this assumption, Eq. (6) can be reduced to

$$\sigma_{ij} = \frac{Gm}{2\pi} \frac{\partial^2}{\partial x_i \partial x_j} \int_S \frac{\Delta\tilde{T}\mathrm{d}x'\mathrm{d}y'}{\sqrt{(x-x')^2+(y-y')^2+z^2}} - 2Gm\Delta T\delta_{ij}\left(\delta_{ix}+\delta_{iy}\right) \tag{7}$$

where $\Delta\tilde{T}$ represents the integral of the temperature change along the direction perpendicular to the fracture plane, that is, $\Delta\tilde{T}(t) = \int_{-\infty}^{+\infty} \Delta T(s,t)\mathrm{d}s$. The second term on the right-hand side of Eq. (7) indicates the stress correction in the x- and y-directions due to the local temperature change (Dontsov, 2021).

Notably, the integral in Eq. (6) has been transformed into a 2D surface integral, which simplifies the model significantly and is similar to the equations for poroelastic stress calculation (Eq. (1)).

The integral of the temperature change along the normal direction of the fracture wall ($\Delta\tilde{T}$) can be expressed as

$$\left.\begin{aligned} &\Delta\tilde{T} = \int_{-\infty}^{+\infty} \Delta T(s,t)\mathrm{d}s = \\ &2\int_0^{+\infty} \sum_{k=1}^{n} \left\{ [f(t_k) - T_0] \left[\operatorname{erfc}\left(\frac{|s|}{\sqrt{4D(t-t_{k-1})}} \right) - \operatorname{erfc}\left(\frac{|s|}{\sqrt{4D(t-t_k)}} \right) \right] \right\} \mathrm{d}s \\ &\Delta\tilde{T}(t) = 4\sqrt{\frac{D}{\pi}} \sum_{k=1}^{n} \left\{ [f(t_k) - T_0] \left[\sqrt{(t-t_{k-1})} - \sqrt{(t-t_k)} \right] \right\} \end{aligned}\right\} \tag{8}$$

3. Numerical method

This section presents the discrete forms of the coupled rock mechanics-fluid flow equations, the convective heat transfer equations within the fractures, and the computational scheme for the thermoelastic stress. The coupling and solution schemes for the entire system are subsequently detailed. For brevity, the discretization of the proppant transport model, the detailed description of the grid system, and the detailed solution process of the coupled rock mechanics-fluid flow equations within the fractures can be found in our previous publications (Wang et al., 2025a, 2025b).

3.1. Discretization form

3.1.1. Discretization of the fluid flow equation

The fluid flow equation is Eq. (3) in Wang et al. (2025b); however, for conciseness, this equation is omitted in this paper. Owing to the varying fluid temperatures at different locations within the fractures, the viscosity also becomes a function of spatial position and time. Therefore, the viscosity should be discretized further when the fluid continuity equations are discretized. In this paper, we present a discrete form that considers the variation in viscosity. The finite difference method is employed to discretize the fluid flow equation. The temporal term is discretized using the first-order backward Euler difference method. For a certain element m, we use the implicit scheme to discretize the equation of fluid flow within fractures, and it is expressed as

$$\left.\begin{aligned} w_m^{(j)} - w_m^{(j-1)} &= \frac{Q_{\text{in}}\Delta t}{(\Delta x)^2}\delta\left(\chi_{\text{inj}} - \chi_m\right) - v_{\text{leak}} - \\ \lambda\sum_{i=1}^{X}\left(\mu_m^{(j)} + \mu_i^{(j)}\right)^{-1}&\left(w_m^{(j)} + w_i^{(j)}\right)^3\left(p_m^{(j)} - p_i^{(j)}\right)H(t-\tau_{0,i}) \\ v_{\text{leak}} = 4C_L\Delta t&\left(\sqrt{t-\tau_{0,m}} - \sqrt{t-\Delta t-\tau_{0,m}}\right)(1-\overline{\phi}), \lambda = \frac{\Delta t}{48(\Delta x)^2} \end{aligned}\right\} \tag{9}$$

where j and $j-1$ in parentheses denote the time step indices, μ_m represents the fluid viscosity for element m, Δt indicates the time step size, X represents the count of neighboring elements of m, i indicates the index of the neighboring elements, and $H(\cdot)$ represents the Heaviside step function.

The fluid pressure of element m can be expressed as

$$p_m = \sigma_m^n + \Delta\sigma_m^{\text{ind}} + \Delta\sigma_m^{\text{poro}} - \Delta\sigma_m^{\text{temp}} \tag{10}$$

where the subscript m denotes the element m; and the first to fourth terms on the right-hand side of the equation indicate the normal in situ stress, stress shadow due to fracture aperture, poroelastic stress, and thermoelastic stress, respectively.

On the basis of the planar hydraulic fracture assumption, the shear displacement discontinuity is zero; thus, the stress shadow due to fracture opening is expressed as (Crouch et al., 1983):

$$\Delta\sigma_m^{\text{ind}} = \sum_{j=1}^{N} A_{\text{nn}}^{mj} D_{\text{n}}^{j} \tag{11}$$

where D_{n}^{j} represents the normal DD of element j, A_{nn}^{mj} represents the DDM influence coefficient, and N represents the number of opened fracture elements.

The poroelastic stress induced by element j at element m is computed by Eq. (1). The computational formula of the thermoelastic stress induced by the source element j is expressed as

$$\Delta\sigma_{zz}^{\text{temp}} = \frac{Gm}{2\pi}\Delta\tilde{T}_j I_{,zz}, I_{,zz} = \frac{\partial^2}{\partial z^2}\int_S \frac{\mathrm{d}x'\mathrm{d}y'}{\sqrt{\left(x-x_j\right)^2 + \left(y-y_j\right)^2 + z^2}} \tag{12}$$

where σ_{zz} indicates the thermoelastic stress in the z-direction, and the calculation for the influence function $I_{,zz}$ can be found in Dontsov (2021).

3.1.2. Discretization of the heat transfer equation

The objective of this subsection is to discretize Eq. (2). Eq. (2) represents a linear advection equation and is formulated as a hyperbolic conservation law, with energy being the conserved quantity. For spatial discretization, a first-order upwind scheme is used; for temporal discretization, a first-order forward Euler difference is applied.

To simplify the expression, we make the following notational simplifications:

$$\frac{\partial(wT)}{\partial t} + \frac{\partial f_x}{\partial x} + \frac{\partial f_y}{\partial y} = 2\frac{\lambda_{\text{r}}}{\rho_{\text{f}} c_{\text{f}}}\frac{\partial T}{\partial n}, f = T\boldsymbol{g}, \boldsymbol{g} = \left(-\frac{w^3}{12\mu}\nabla p\right)Q_{\text{s}}(\overline{\phi}) \tag{13}$$

Because we have employed a structured orthogonal grid, the discretization forms for the x- and y-directions are identical; thus, we have the following explicit scheme:

$$\frac{w_{i,j}^{n+1}T_{i,j}^{n+1} - w_{i,j}^{n}T_{i,j}^{n}}{\Delta t} = \frac{f_{x,(i+1/2,j)}^{n} - f_{x,(i-1/2,j)}^{n}}{\Delta x} + \frac{f_{y,(i,j+1/2)}^{n} - f_{y,(i,j-1/2)}^{n}}{\Delta y} + 2\frac{\lambda_{\text{r}}}{\rho_{\text{f}} c_{\text{f}}}\frac{\partial T}{\partial n} \tag{14}$$

where the subscripts i and j denote the element indices, n and $n+1$ indicate the time step indices, and the temperature gradient at the fracture wall can be calculated by Eq. (5).

The first-order upwind scheme is applied, yielding the expression for the heat flux at the interface (with $f_{x,i+1/2}$ as an example) as

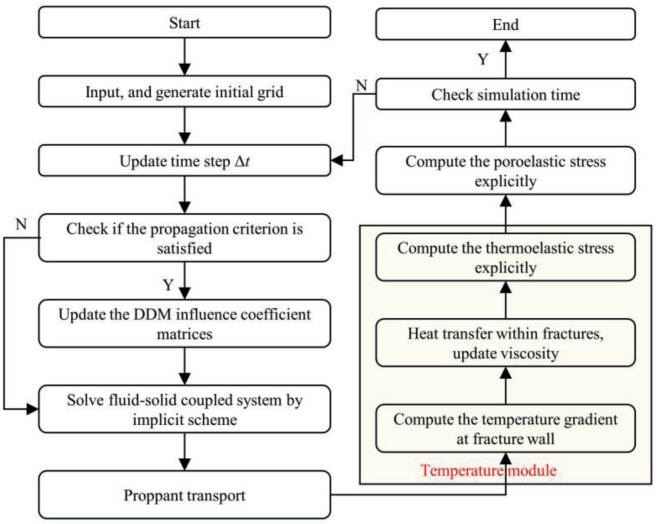

Fig. 3. Workflow of the current model.

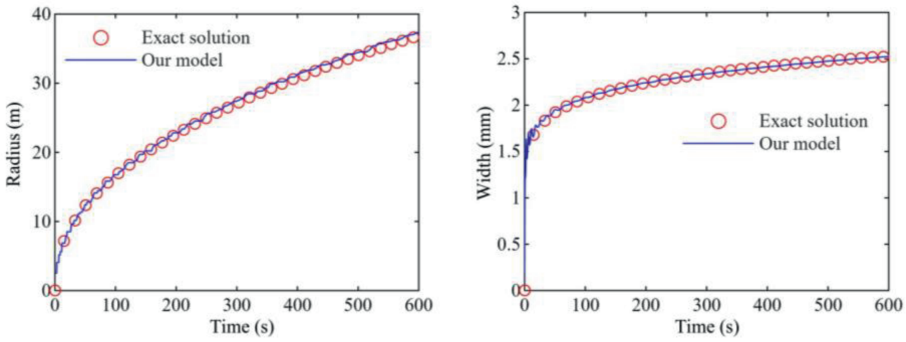

(a) Comparison of fracture radius (b) Comparison of fracture width

Fig. 4. Validation results of fracture propagation.

$$\left.\begin{aligned} f_{x,(i+1/2,j)} &= T_{i,j}g_{i+1/2,j}H\left(g_{i+1/2,j}\right) + T_{i+1,j}g_{i+1/2,j}H\left(-g_{i+1/2,j}\right) \\ g_{i+1/2,j} &= -\frac{\left(w_{i,j}+w_{i+1,j}\right)^3\left(p_{i+1,j}-p_{i,j}\right)}{48\left(\mu_{i,j}+\mu_{i+1,j}\right)\Delta x} \end{aligned}\right\} \tag{15}$$

where $H(\cdot)$ denotes the Heaviside step function.

3.2. Workflow

Fig. 3 presents the calculation flowchart for the integrated simulation of fracture propagation, proppant transport, heat transfer, poroelastic stress, and thermoelastic stress. The fluid-solid coupling equations are solved using an implicit method, whereas the proppant transport and temperature transfer within the fracture are addressed using an explicit method. Because the implicit algorithm is unconditionally stable, the time step Δt for fracture propagation may be relatively large, which does not meet the stability requirements for an explicit scheme of proppant transport and the temperature field within the fracture. Therefore, to determine the temperature field and proppant transport within a fracture, we subdivide the fracture propagation time step Δt to satisfy the stability condition of the explicit scheme. For additional details on fracture propagation and proppant transport modeling, see our previous paper (Wang et al., 2025a, 2025b).

4. Model validation

This section presents the validation results of the proposed fracture propagation and heat transfer model. In Section 4.1, our results are validated with the analytical solution for a penny-shaped fracture (Dontsov, 2016). Section 4.2 presents the validation results of the temperature distribution within fractures against the exact solution from Lowell (1976).

4.1. Validation for fracture propagation

The model parameters for validating fracture propagation are obtained from Wang et al. (2025a). As shown in Fig. 4, the temporal evolution of the fracture radius and inlet width shows excellent agreement with the analytical solution (Dontsov, 2016). For more comprehensive verification cases, please refer to our previously published papers (Chen et al., 2020; Wang et al., 2025a, 2025b).

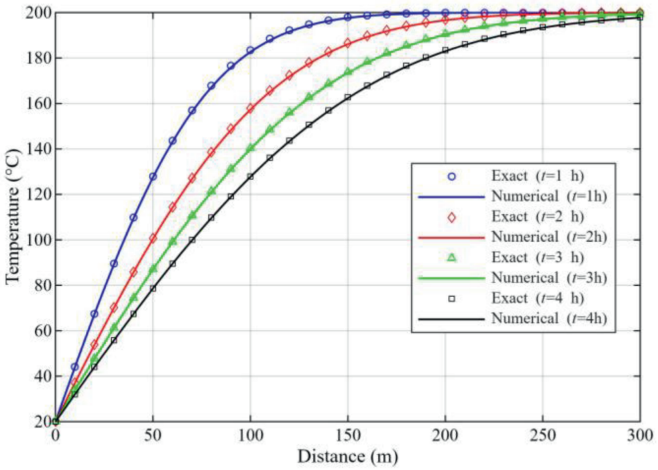

Fig. 5. Validation results of heat transfer within hydraulic fractures.

4.2. Validation of heat transfer

During fracture propagation, the fracturing fluid undergoes continuous thermal exchange with adjacent rock formations, resulting in an increase in fluid temperature and a decrease in rock temperature. This coupling process was validated against an analytical solution (Lowell, 1976). We compared the temporal evolution of the fluid temperature distribution within the fracture with the established exact solution.

$$T(z,t) = T_{\text{inj}} + \left(T_0 - T_{\text{inj}}\right)\text{erf}\left(\frac{z}{c_{\text{f}}\rho_{\text{f}}v_{\text{f}}w}\sqrt{\frac{\lambda_{\text{r}}c_{\text{r}}\rho_{\text{r}}}{t}}\right) \tag{16}$$

The input parameters are as follows: the initial reservoir temperature T_0 is 200 °C, the injection fluid temperature T_{inj} is 20 °C, the thermal conductivity of the reservoir rock λ_{r} is 2.8 W/(°C m), the density of the reservoir rock ρ_{r} is 2600 kg/m^3, the specific heat capacity of the reservoir rock c_{r} is 1000 J/(kg °C), the density of the injection fluid ρ_{f} is 1000 kg/m^3, the specific heat capacity of the injection fluid c_{f} is 4200 J/(kg °C), the velocity of the fluid v_{f} is 0.3 m/s, and the fracture width w is 3 mm. In Eq. (5), the pressure gradient is an alternative representation of the fluid velocity, and the derivation is not repeated in this paper.

Fig. 5 presents the comparison results of fluid heat transfer within a fracture against the exact solution. The results from our model are almost identical to the exact solution, indicating that the model and the computational code developed in this study are highly accurate.

Table 1
Input parameters for a propagating penny-shaped fracture.

Parameter	Unit	Value
Young's modulus	GPa	30
σ_h	MPa	90
Poisson's ratio		0.2
Fracture toughness	MPa $m^{0.5}$	0.5
Rock density	kg/m^3	2600
Initial rock temperature	°C	150
Specific heat of rock	J/(kg °C)	1000
Rock heat conductivity	W/(°C m)	3
Thermal expansion coefficient	$°C^{-1}$	5×10^{-6}
Carter's leak-off coefficient	m/$min^{0.5}$	10^{-4}
Reference viscosity (μ_{ref})	mPa s	10
Fluid temperature (T_{ref})	°C	30
Injection rate	m^3/min	0.6
Specific heat of fluid	J/(kg °C)	4200
Temperature sensitivity coefficient of fluid (C_T) (Tang et al., 2016; Lin et al., 2024)	$°C^{-1}$	0.02
Simulation time	min	10

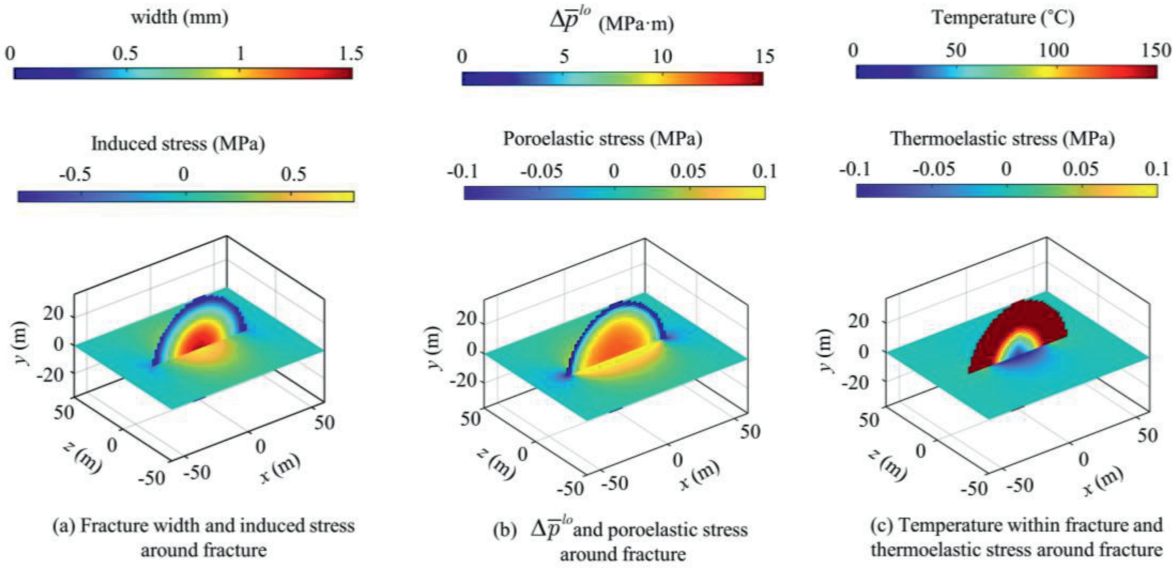

Fig. 6. Fracture-induced stress, poroelastic stress, and thermoelastic stress distributions around a penny-shaped fracture.

5. Analysis of fracture propagation considering thermal effects

This section investigates the thermal effects for a propagating penny-shaped hydraulic fracture, focusing on the thermoelastic stress and the VTE of the fracturing fluid. Initially, using the parameters in Table 1 and disregarding the VTE, Section 5.1 examines the stress distribution and fracture propagation dynamics under four scenarios: pure elastic, poroelastic, thermoelastic, and thermoporoelastic. Section 5.2 subsequently examines the VTE by excluding poroelastic and thermoelastic effects and analyzes the impact of the VTE on fracture propagation in both viscosity-dominated (*M*-) and toughness-dominated (*K*-) regimes via comparative studies. Section 5.3 evaluates the competitive relationship between the VTE and the thermoelastic effect on fracture propagation, determining the dominant factor in both the *M*- and *K*-regimes. This systematic analysis provides comprehensive insights into the effect of temperature on hydraulic fracture growth.

5.1. Thermal stress analysis of a propagating penny-shaped fracture

This subsection analyzes the thermoelastic effect and compares the results of fracture propagation with those of purely elastic, poroelastic, and thermoporoelastic cases. This subsection also examines the distribution range and magnitude of several induced stresses around the fracture. These induced stresses include fracture-induced stress, poroelastic stress, and thermoelastic stress. The fracture-induced stress represents the stress induced by the opening of the fracture in the surrounding area, the poroelastic stress is the stress variation caused by the leakage of fracturing fluid into the formation pores, and the thermoelastic stress is the stress variation caused by temperature changes. The input parameters are listed in Table 1.

Fig. 6 presents the fracture geometry and spatial distribution of three types of stresses in the surrounding rock: fracture-induced stress, poroelastic stress, and thermoelastic stress. Fracture-induced stress, generated by fracture opening, has the highest magnitude (approximately 0.8 MPa) and imposes compressive loading on the adjacent rock. Poroelastic stress, induced by fluid leakage into the formation, ranges between 0.1 and 0.2 MPa. This stress component arises from pore pressure buildup due to fluid leakage, resulting in pore expansion and subsequent rock compression, thereby contributing to compressive stress. The thermoelastic stress (approximately 0.1 MPa) exhibited contrasting behavior. The injection of cold fluid induces rapid cooling and

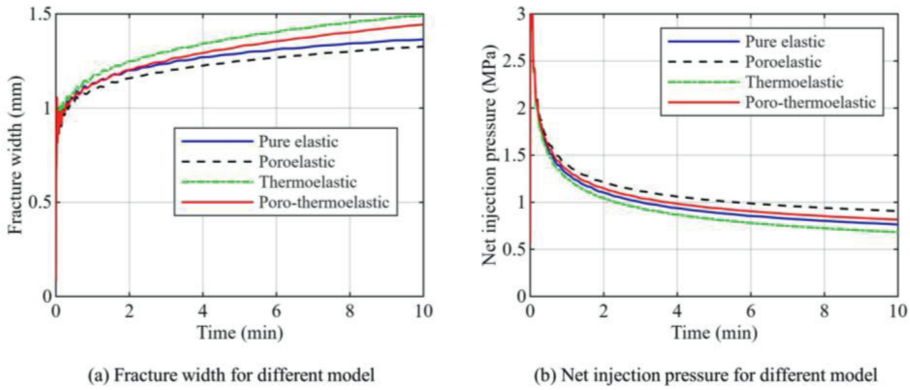

(a) Fracture width for different model (b) Net injection pressure for different model

Fig. 7. Variations in the fracture inlet width and net injection pressure over time for different models.

contraction of the rock near the fracture, reducing local in situ stress and generating tensile stress. Consequently, while fracture-induced and poroelastic stresses increase compressive loading, thermoelastic stress counteracts this effect by tensile stress, thereby reducing the in situ stress.

To investigate fracture propagation dynamics, we conducted a comparative analysis of four types of models: purely elastic, poroelastic, thermoelastic, and thermoporoelastic (Fig. 7). As shown in Fig. 7a, the fracture inlet width is remarkably different for the different models. The thermoelastic model yields the largest width (1.5 mm), followed by the thermoporoelastic model (1.4 mm). In contrast, the purely elastic model produces a width of 1.3 mm, whereas the poroelastic model results in the narrowest fracture (1.25 mm). These findings reveal that thermoelastic effects facilitate fracture opening, whereas poroelastic mechanisms limit it. Notably, the thermoporoelastic model generates a wider fracture than the purely elastic model does, indicating that—for the given parameters (Table 1)—thermal stresses have a more dominant influence on fracture aperture than poroelastic effects do.

Fig. 7b shows the variation in the net injection pressure with time for several models. The injection pressure considering poroelastic effects is the highest, whereas that considering only thermoelasticity is the lowest. The injection pressure considering thermoporoelasticity lies between these two extremes but is slightly higher than that in the purely elastic case. This finding indicates that for the parameters listed in Table 1, the effect of poroelasticity on the net injection pressure is more significant than that of thermoelasticity.

The analysis reveals that thermoelastic and poroelastic effects fundamentally oppose fracture behavior: thermoelasticity increases the inlet fracture width and reduces the injection pressure, whereas poroelasticity decreases the fracture width and increases the pressure. Fig. 8 shows the spatial evolution of the fracture width and net pressure along the fracture radius (x direction). The results clearly show zonal characteristics. Near the injection point (x < 22 m), the thermoelastic model produces larger fracture widths than the purely elastic model does because of pronounced cooling-induced rock contraction, whereas the two models converge at distances greater than 22 m as the fluid temperature gradually equilibrates with the formation temperature, and the thermoelastic effects are negligible. In contrast, poroelastic effects uniformly reduce the fracture width relative to the elastic case throughout the fracture length scale. This divergence stems from differing mechanisms: fluid leak-off has a continuous poroelastic effect, whereas thermal exchange decreases with distance as the fluid approaches thermal equilibrium at positions near the fracture front. In other words, fluid leak-off occurs at any position of fracture, whereas heat exchange only occurs in the high-temperature difference area. The thermoporoelastic model exhibits transitional dominance: thermoelastic effects are more dominant in the near-wellbore region where the temperature difference is large, yielding wider fractures than those in the elastic case, whereas poroelastic effects are dominant in the fracture front region where the temperature difference is near zero, resulting in a narrower width that is consistent with the

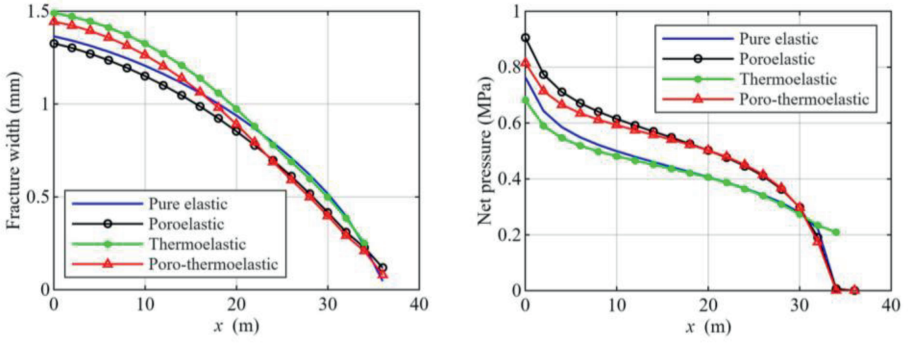

(a) Fracture width for different model (b) Net pressure for different model

Fig. 8. Variations in fracture width and net pressure with radius for different models.

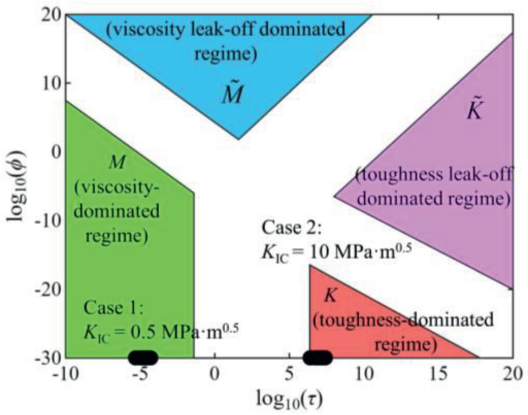

Fig. 9. Distribution of the two cases in the parametric space of a penny-shaped fracture.

poroelastic model. These zonal characteristic spatial transitions indicate that there is a competitive relationship between poroelasticity and thermoelasticity. In the net pressure distribution curves shown in Fig. 8b, the net pressure distribution curve considering the thermoelastic effect is significantly lower than that of the purely elastic case near the injection point, whereas it is similar to the purely elastic case at the fracture front. This finding is consistent with the phenomenon shown in Fig. 8a. Additionally, the pressure drop from the injection point to the fracture front for the thermoelastic case is relatively small compared with the results of the purely elastic condition. Combined with the characteristics of a larger fracture width and lower fluid flow resistance, the energy consumed to overcome fluid flow resistance has decreased, so we speculate that the thermoelastic effect may cause the fracture to tend toward a toughness-dominated feature. In contrast, the poroelastic effect increases the net pressure. Because the moment of fluid leak-off begins earlier near the injection point, the poroelastic stress in this region is greater than that of the fracture front, which increases the pressure difference from the injection point to the fracture front. Combined with the characteristics of a smaller fracture width and higher fluid flow resistance, the energy consumed to overcome fluid flow resistance has increased, and we reasonably infer that the poroelastic effect may cause the fracture to tend toward a viscosity-dominated feature.

5.2. Analysis of a propagating penny-shaped fracture with a VTE

In the previous subsection, we analyzed the differences among several types of stresses and the impact of different mechanisms on fracture propagation. However, the thermal effect for a propagating hydraulic fracture is not limited to the thermoelastic stress but also includes the VTE. Therefore, in this section, we use the parameters in Table 1 but do not consider fluid leak-off, the poroelastic effect, or the thermoelastic effect. We investigate the impact of the VTE on fracture propagation under both the *M*- and *K*-regimes.

Fig. 9 presents two scenarios for penny-shaped fractures, which represent two different propagation regimes. Case 1 corresponds to the *M*-regime, characterized by predominant energy dissipation through fluid flow. Conversely, Case 2 indicates the *K*-regime, where the majority of energy is used to fracture rocks and form new fracture surfaces.

For the *M*-case, Fig. 10a and b shows the fluid viscosity and temperature distributions within the hydraulic fracture. The viscosity is greater near the injection point due to the lower temperature, whereas it is lower at the fracture front where the temperature is higher. Notably, viscosity is highly sensitive to temperature changes. At a fracture radius of approximately

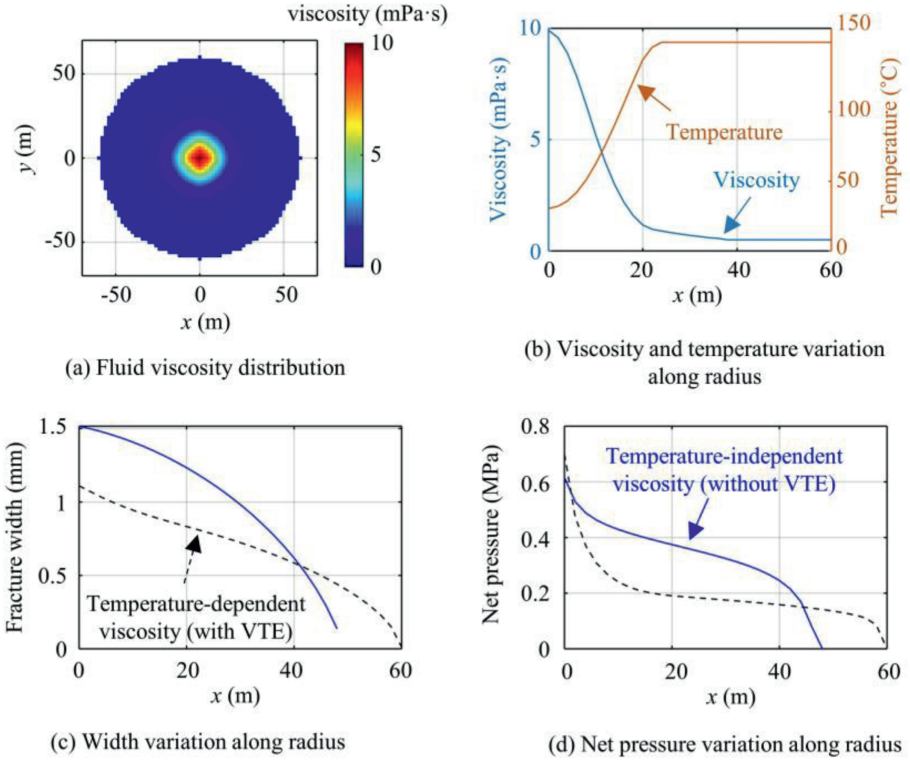

(a) Fluid viscosity distribution

(b) Viscosity and temperature variation along radius

(c) Width variation along radius

(d) Net pressure variation along radius

Fig. 10. Fracture propagation results with and without considering the VTE (Case 1, within the *M*-regime).

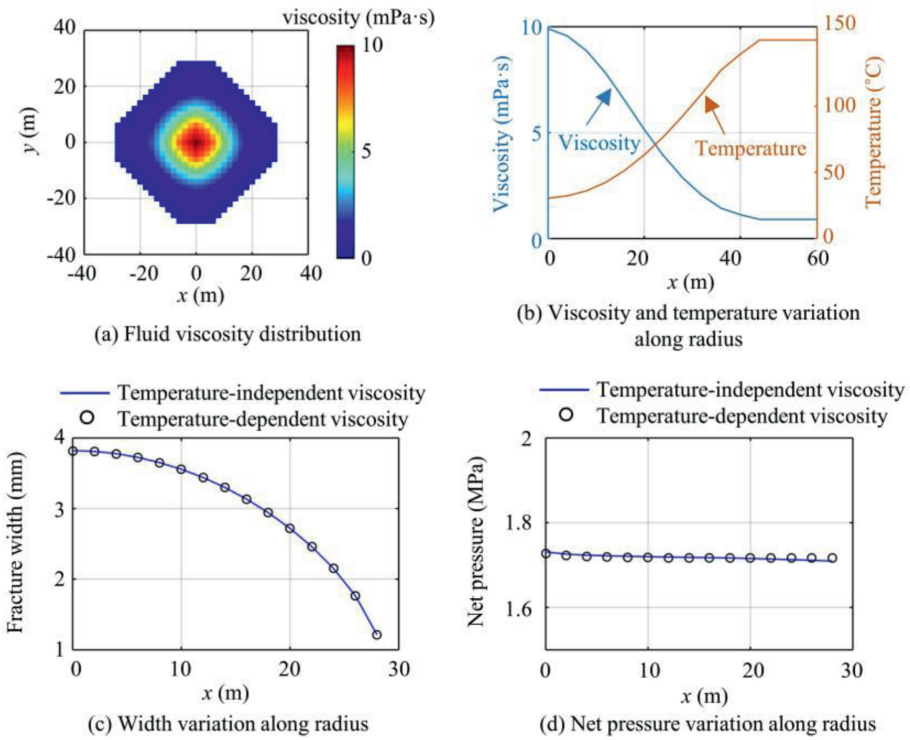

Fig. 11. Fracture propagation results with and without considering the VTE (Case 2, within the *K*-regime).

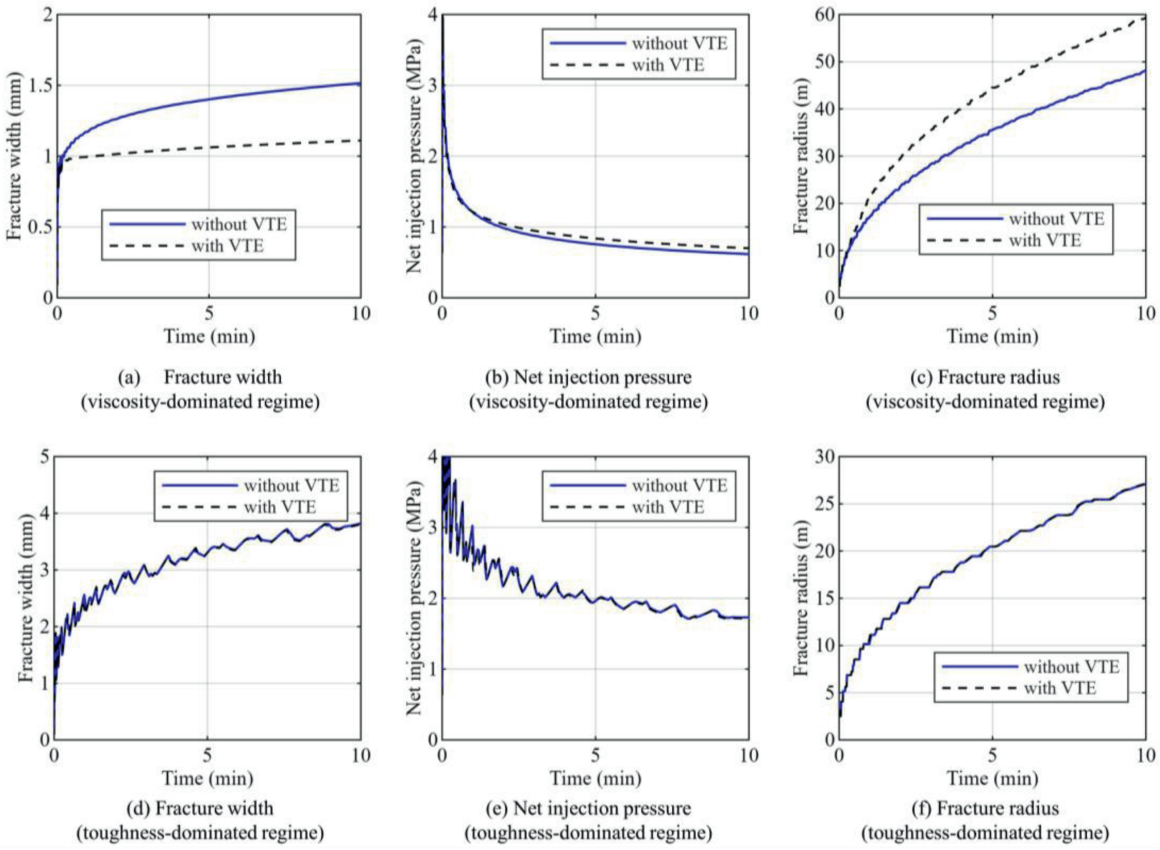

Fig. 12. Fracture width, net injection pressure, and fracture radius versus time with and without considering the VTE.

$x = 20$ m, the fluid viscosity has already decreased by approximately 80 %. In the region of $x = 20$–60 m, the fluid temperature within the fracture is near the initial rock temperature, thus the viscosity change is not significant.

The analysis of fracture width and pressure distribution in Fig. 10c and d reveals significant differences induced by VTEs. When the VTE is considered, the maximum fracture width decreases by approximately 27 % (from 1.5 mm to 1.1 mm), whereas the fracture radius increases by 36 % (from 44 m to 60 m). This inverse relationship between width reduction and radial velocity stems from thermally induced viscosity reduction, which simultaneously decreases the net pressure while increasing fluid mobility. Under constant-volume and no leak-off conditions, the reduced viscosity results in a greater fracture radius and a smaller fracture width. The pressure profiles exhibit distinctive characteristics, particularly in the fracture front regions ($x > 20$ m). The case with the VTE shows an obvious "pressure plateau", which contrasts with the sharp gradient observed in the case without the VTE. This phenomenon arises from thermal equilibration at the fracture front, where elevated temperatures reduce fluid viscosity substantially. Consequently, fracture propagation may transition to toughness-dominated behavior, stabilizing the pressure gradient as energy dissipation becomes governed primarily by fracturing the rock fracture rather than viscous flow.

Under the *K*-regime, the distributions of viscosity and temperature within the fracture zone are consistent with those in the *M*-regime. The difference is that, for the *K*-regime, the influence of with or without a VTE on the fracture width and net pressure is minimal, as shown in Fig. 11c and d. Most of the energy of the injected fluid is used to fracture the rock, and the effect of the reduction in fluid viscosity is not significant, although a slight difference is observed. For example, in Fig. 11d, the net pressure distribution curve without a VTE has a very small slope, whereas the slope decreases when the VTE is considered. This phenomenon can be identified at the intersection of the curve and the circles in Fig. 11d.

Fig. 12 shows the variations in the fracture inlet width, net injection pressure, and fracture radius under the *M*- and *K*-regimes. Like the analysis presented earlier, the VTE influences fracture propagation primarily in the *M*-region, whereas its impact on fracture propagation in the *K*-region is not significant. Notably, under toughness-dominated conditions, several curves exhibit zig-zag oscillation. According to Chen et al. (2020), fracture propagation is relatively difficult under toughness conditions, and there is a stage of pressure accumulation before propagation occurs and a stage of sudden release after propagation occurs, i.e. the "storage" process and "release" process, respectively.

5.3. Comparison of the effects of thermoelastic stress and the VTE on hydraulic fracture propagation

Building upon our previous analyses of thermoelasticity and VTE in the previous sections, which examined their influences on fracture propagation in different propagation regimes, this section conducts a comprehensive comparative study. We systematically evaluate the thermoelasticity and VTE in governing fracture evolution, with particular emphasis on quantifying their respective contributions to fracture geometry and propagation dynamics.

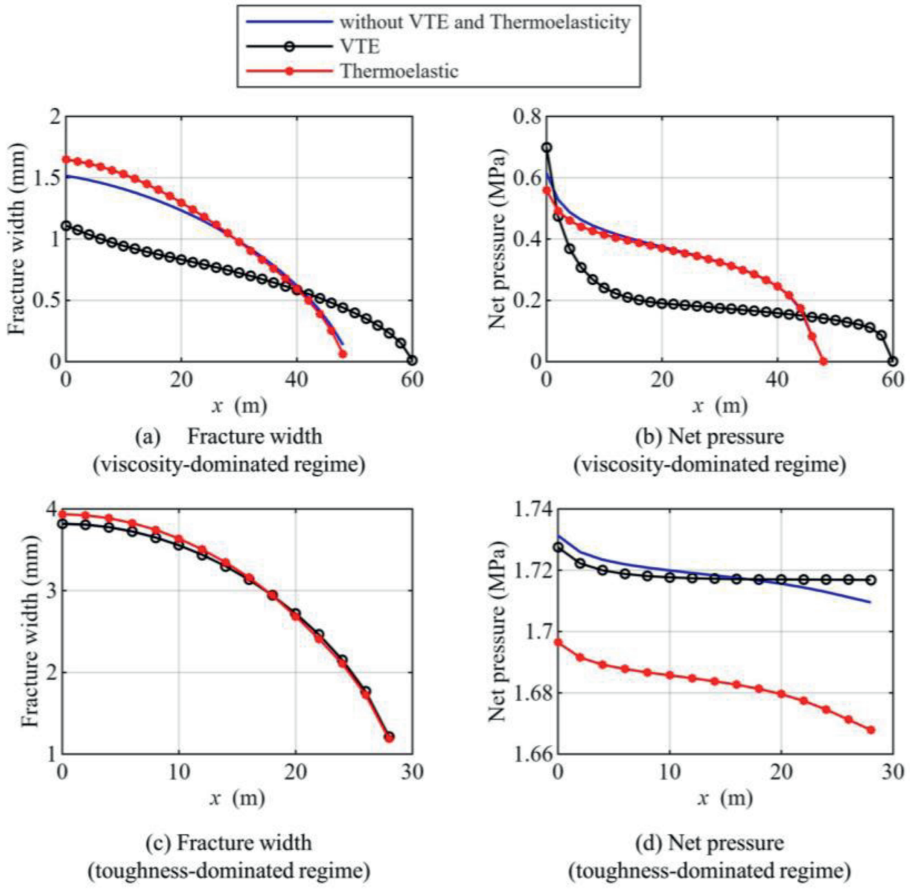

Fig. 13. Comparison of the effects of thermal stress and temperature-dependent viscosity in the *M*- and *K*-regimes.

Fig. 13 compares the effects of thermoelasticity and the VTE on fracture propagation in the *M*- and *K*-regimes. Under the *M* regime (Fig. 13a and b), compared with disregarding thermal stress and the VTE, thermoelastic stress slightly affects the fracture width and injection pressure, with specific manifestations consistent with the analysis in Section 5.1. When the VTE is considered and thermoelasticity is disregarded, the changes in fracture width and pressure are consistent with the analysis in Section 5.2. However, a comparison of the two reveals that in the *M*-regime, the influence of the VTE on fracture propagation is much greater than that of thermoelasticity, with both the fracture width and net pressure within the fracture being significantly reduced. In contrast, under the *K*-regime (Fig. 13c and d), the VTE has almost no impact on the fracture width and injection pressure, with specific manifestations consistent with the analysis in Section 5.2. In contrast to Fig. 13a and b, the influence of thermoelasticity is significantly greater than that of the VTE in this case, with thermoelasticity being dominant, but it has a very small value.

6. Discussion

This paper investigates the impact of thermal effects on fracture propagation. Detailed analyses of fracture propagation are conducted under both *M*- and *K*-regimes. The influences of thermoelasticity and the VTE on fracture propagation are compared between the two propagation regimes. Considering only thermoelasticity, we find that thermal stress can increase the fracture width and decrease the injection pressure, which is consistent with the conclusions drawn by Wang et al. (2024a). Moreover, when thermoporoelastic effects are considered, both thermal and poroelastic effects are significant near the injection point and exhibit competitive interactions (Fig. 8). This competitive interaction is determined by the strength of fluid leak-off, the intensity of heat conduction, and the reservoir properties. At the fracture front far from the injection point, the temperature difference between the fracturing fluid within the hydraulic fracture zone and the formation rock is relatively small, whereas the pressure difference remains large. Therefore, the thermal elastic effect can be disregarded, and the poroelastic effect is more remarkable. Overall, for short-duration treatments, such as hydraulic fracturing, the range and degree of influence of the poroelastic effect may be greater. In their research on long-term water injection development of improved geothermal systems, Ghassemi and Zhou (2011) reported that the poroelastic effect initially dominated, whereas the thermal elastic effect dominated later, which is also consistent with our research results.

When thermoelasticity and poroelasticity are disregarded and only the VTE of the fluid is considered, we find that, compared with the case without VTE, the fracture width is significantly reduced, whereas the fracture length is significantly increased.

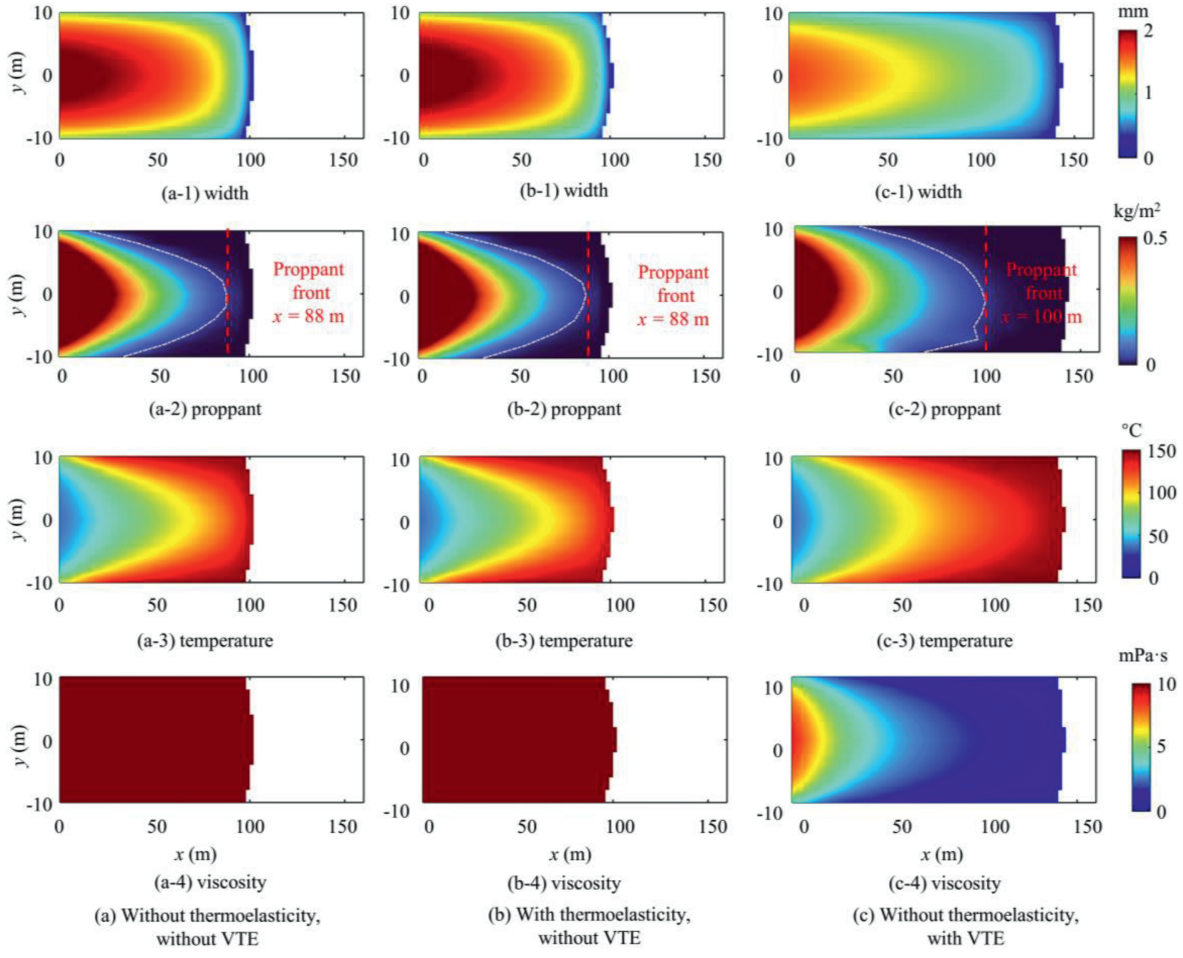

Fig. 14. Fracture propagation and proppant transport results for different conditions. The proppant diameter is 200 μm. The left column represents the pure elastic model, the middle column represents the thermoelastic model, and the right column represents the model that considers the VTE but does not consider thermoelasticity. The first row to the fourth row represent the fracture width, proppant concentration, temperature, and viscosity distribution.

Tang et al. (2016) also reached this conclusion. This phenomenon is particularly remarkable in the *M*-regime, whereas there is almost no change in the *K*-regime. This result is determined by energy dissipation during fracture propagation, as analyzed by Detournay (2004). We believe that this conclusion is instructive for actual field operations. According to Adachi et al. (2007), Lecampion et al. (2018), and Lecampion and Desroches (2015), under actual field conditions, fractures generally propagate in the *M*-regime, thus the VTE may be significant.

Additionally, on the basis of the analysis in Section 5, the thermal effect has a considerable influence on fracture propagation, and it undoubtedly influences proppant transport. Liu et al. (2025) simulated proppant transport in a geothermal reservoir fracture network while considering the thermal effect and reported that the thermal effect resulted in a reduction in fluid viscosity and an increase in the proppant settling velocity, thereby reducing the proppant transport distance and the propped area. However, Liu et al. (2025) used a static fracture network and did not consider fracture propagation, so this conclusion may have certain limitations. To verify this conclusion, we appropriately extend the research content of this paper. The specific parameters used for fracture propagation are shown in Table 1. However, we do not consider fluid leak-off, and the fracture geometry is restricted to a constant-height (22 m) fracture model with proppant particle sizes of 200 μm and 350 μm. Proppant injection begins at the 3rd minute, and the pumping schedule is a stepwise increase, starting at 50 kg/m^3 and increasing by 50 kg/m^3 every minute, up to 350 kg/m^3. Detailed descriptions of proppant transport can be found in our previous research (Wang et al., 2025b).

Fig. 14 presents the results with a 200 μm proppant particle size, including the results without thermoelasticity and VTE, only considering thermoelasticity, and only considering VTE. A comparison of Fig. 14a and b reveals that the differences in fracture propagation and proppant transport results with and without thermoelasticity are not obvious. However, a comparison of Fig. 14a and c reveals that these differences are significant. The fracture length in Figs. 14c–1 is approximately 40 m longer than those in Figs. 14a–1 and b-1, and the proppant transport distance is also significantly greater (Figs. 14c–2). When the VTE is considered, the overall viscosity of the fluid decreases, resulting in a longer fracture length and a longer transport distance for the small proppant particles. Additionally, there is a noticeable proppant settling in Figs. 14c–2, which is also related to the reduced fluid viscosity. However, as shown in Fig. 15, when a large proppant (350 μm in diameter) is used, the results are opposite those of the small proppant particles in Fig. 14. In this case, the proppant transport distance is shorter when the VTE is considered (Figs. 15c–2) because the decrease in viscosity also results in a significant reduction in fracture width. Moreover, owing to the

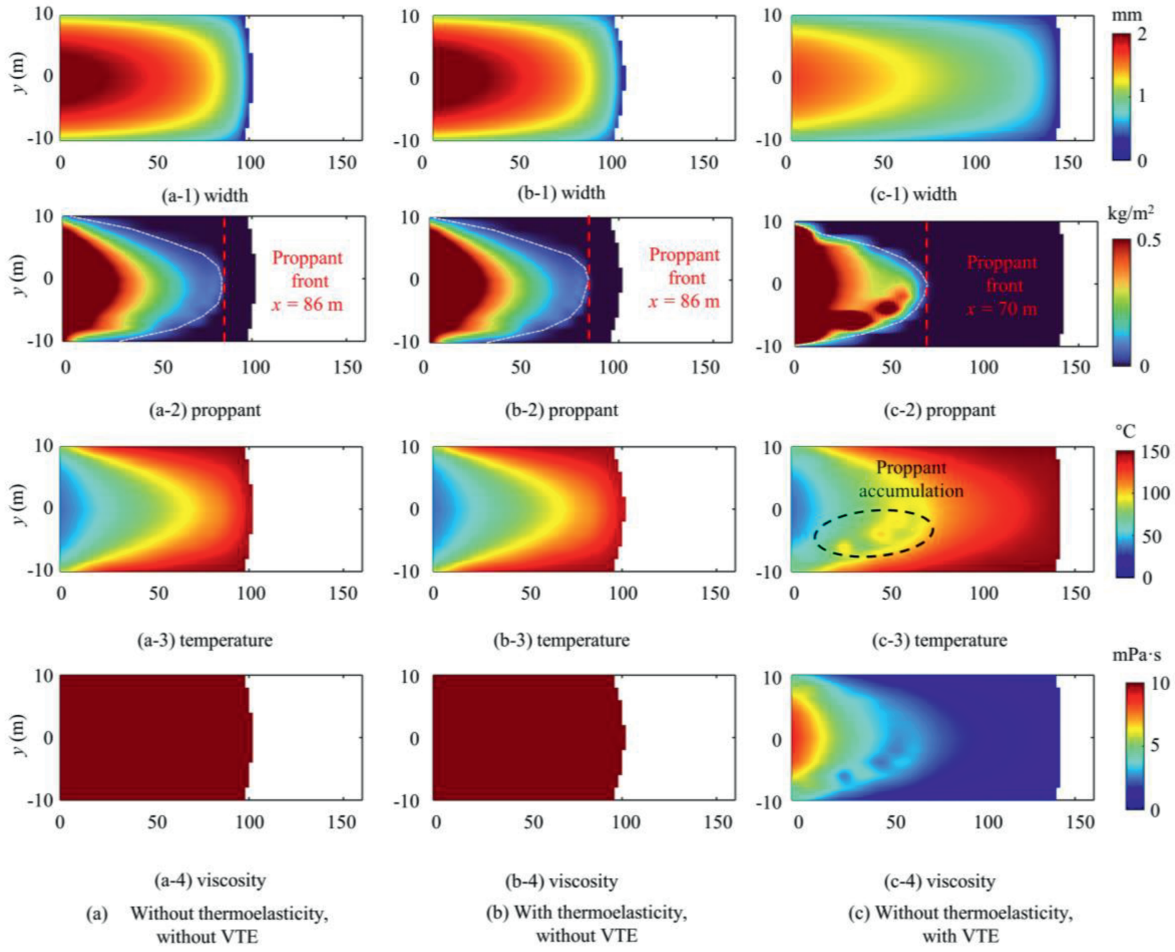

Fig. 15. Fracture propagation and proppant transport results for different conditions. The proppant diameter is 350 μm. The leftmost column represents the pure elastic model, the middle column represents the thermoelastic model, and the rightmost column represents the model that considers the VTE but does not consider thermoelasticity. The first row to the fourth row represent the fracture width, proppant concentration, temperature, and viscosity distribution.

high proppant concentration in the narrow fracture width area and the decrease in the slurry flow velocity, a local high temperature appears where the proppant particles accumulate (Figs. 15c–3), which also appears in Tang et al. (2016).

The thermoelastic effect has a negligible effect on both fracture propagation and proppant transport, but the impact of the VTE on proppant transport is more remarkable. Although the VTE causes the proppant to settle more rapidly, it is not necessarily always detrimental. For small proppant particles, thermal effects can increase the fracture length, increase the proppant transport distance, and increase the propped area. In contrast, for large proppant particles, thermal effects can hinder the transport of proppant particles toward the fracture front and cause significant sedimentation.

For fracturing deep reservoirs, in addition to the proppant size, the properties of the fracturing fluid, especially the VTE of the fracturing fluid, deserve more attention. We believe that when the fracturing fluid viscosity is insensitive to temperature, the VTE of the fluid becomes less significant, and the thermoelastic stress begins to dominate. When the fracturing fluid viscosity is highly sensitive to temperature, the VTE of the fluid becomes substantial, and VTE dominates. When the fracturing fluid viscosity has a moderate sensitivity to temperature, the thermoelastic effect and VTE are in competition. In addition, the potential damage of the fracturing fluid to deep reservoirs should also be considered. Therefore, an appropriate fracturing fluid system should be selected on the basis of the sensitivity of the actual reservoir. To avoid a sharp decrease in fluid viscosity under high-temperature conditions, which causes rapid proppant settling, a fracturing fluid system that is insensitive to temperature should be selected, or a high injection rate should be applied to reduce the proppant settling velocity and increase the proppant transport distance. Small proppants should be used as much as possible to increase both the transport distance of the proppants and production. This conclusion may provide some insights into hydraulic fracturing design in deep and ultradeep oil, gas, and geothermal reservoirs.

Some limitations in this work are as follows: In considering the heat exchange between the fracturing fluid within the hydraulic fractures and the formation rock, to obtain analytical solutions more easily (Eqs. (4) and (5)), we disregard the heat transfer due to fluid leak-off, which may result in inaccurate changes in rock temperature. In addition, owing to the assumption of 1D pressure and temperature diffusion, the method for determining the temperature distribution, thermal stress, and poroelastic stress can be applied only to relatively short duration processes, such as hydraulic fracturing, and is not suitable for long-term production processes. In future research, we will address these issues and conduct more refined dimensionless analysis, thereby clearly guiding deep reservoir fracturing.

7. Conclusions

Building upon our established fracture propagation and proppant transport framework (Wang et al., 2025a, 2025b), this study presents an improved hydraulic fracturing model for deep reservoirs by incorporating poroelastic and thermal coupling mechanisms. The developed model enables comprehensive investigation of three critical factors, i.e. poroelastic stress, thermoelastic stress, and VTE, in penny-shaped fracture development. Through systematic analysis, we quantify and compare the relative contributions of thermoelasticity and the VTE under both viscosity-dominated and toughness-dominated propagation regimes. Furthermore, we extend our examination to proppant transport dynamics, evaluating how thermal effects influence the particle distribution within fractures. Key findings include the following:

(1) Thermal stress exhibits behavior opposite that of poroelastic stress, reducing the injection pressure and increasing the fracture width.
(2) Under viscosity-dominated conditions, the effect of thermoelastic stress on fracture propagation is relatively weak, whereas the VTE is more pronounced. In contrast, under toughness-dominated conditions, the results are reversed; however, the effect of thermoelastic stress on fracture propagation remains relatively weak (although not negligible), whereas the VTE can essentially be disregarded.
(3) When proppant transport is considered, for small proppant particles, the transport distance increases when the VTE is considered. The proppant transport distance increases from 84 m to 100 m. In contrast, for large proppant particles, owing to the decrease in viscosity with increasing temperature, the transport distance is significantly reduced. The proppant transport distance decreases from 80 m to 64 m. This finding indicates that in deep reservoir fracturing, reasonable selection of the proppant size ensures a high fracture conductivity and propped area and the VTE of the fracturing fluid deserves more attention.

CRediT authorship contribution statement

Yunpeng Wang: Writing – original draft, Visualization, Validation, Software, Methodology, Investigation, Formal analysis, Data curation, Conceptualization. **Ming Chen:** Writing – original draft, Visualization, Validation, Software, Methodology, Investigation. **Tiankui Guo:** Visualization, Validation, Investigation. **Jiwei Wang:** Visualization, Conceptualization. **Bo Zhang:** Visualization, Conceptualization. **Zhanqing Qu:** Formal analysis.

Declaration of competing interest

The authors declare that they have no known competing financial interests or personal relationships that could have appeared to influence the work reported in this paper.

Acknowledgments

We acknowledge the financial support of the Basic Science Center Project of the National Natural Science Foundation of China (Grant No. 52288101) “Flow Control of Ultra-deep and Extra-deep Oil and Gas Drilling and Production”.

Appendix A. Supplementary data

Supplementary data to this article can be found online at https://doi.org/10.1016/j.jrmge.2025.07.027.

References

Adachi, J., Siebrits, E., Peirce, A., Desriches, J., 2007. Computer simulation of hydraulic fractures. Int. J. Rock Mech. Min. Sci. 44 (5), 739–757.
An, M., Huang, R., Elsworth, D., Zhang, F., Dontsov, E., 2025. Thermoporoelastic stress perturbations from hydraulic fracturing and thermal depletion in enhanced geothermal systems (EGS) and implications for fault reactivation and seismicity. J. Rock Mech. Geotech. Eng. 17 (5), 2893–2903.
Carter, E., 1957. Optimum fluid characteristics for fracture extension. In:

Howard, G.C., Fast, C.R. (Eds.), Drilling and Production Practices. American Petroleum Institute, Tulsa OK, pp. 261–270.
Chen, M., Zhang, S., Li, S., Ma, X., Zhang, X., Zou, Y., 2020. An explicit algorithm for modeling planar 3D hydraulic fracture growth based on a super-time-stepping method. Int. J. Solid Struct. 191–192, 370–389.
Chen, M., Guo, T., Zou, Y., Zhang, S., Qu, Z., 2022a. Numerical simulation of proppant transport coupled with multi-planar-3D hydraulic fracture propagation for multi-cluster fracturing. Rock Mech. Rock Eng. 55 (2), 565–590.
Chen, M., Guo, T., Xu, Y., Qu, Z., Zhang, S., Zhou, T., Wang, Y., 2022b. Evolution mechanism of optical fiber strain induced by multi-fracture growth during fracturing in horizontal wells. Petrol. Explor. Dev. 49 (1), 211–222.
Chen, H., Kang, Y., Jin, W., Li, C., Cai, C., 2024. Numerical modeling of fracture propagation of supercritical CO_2 compound fracturing. J. Rock Mech. Geotech. Eng. 16 (7), 2607–2628.
Crouch, S., Starfield, A., Rizzo, F., 1983. Boundary Element Methods in Solid Mechanics.
Dontsov, E., 2016. An approximate solution for a penny-shaped hydraulic fracture that accounts for fracture toughness, fluid viscosity and leak-off. R. Soc. Open Sci. 3 (12), 160737.
Dontsov, E., 2021. An efficient computation of leak-off induced poroelastic stress for a hydraulic fracture. J. Mech. Phys. Solid. 147, 104246.
Detournay, E., 2004. Propagation regimes of fluid-driven fractures in impermeable rocks. Int. J. GeoMech. 4 (1), 35–45.
Ghassemi, A., Tarasovs, S., Cheng, A., 2005. Integral equation solution of heat extraction-induced thermal stress in enhanced geothermal reservoirs. Int. J. Numer. Anal. Methods GeoMech. 29, 829–844.
Ghassemi, A., Zhou, X., 2011. A three-dimensional thermo-poroelastic model for fracture response to injection/extraction in enhanced geothermal systems. Geothermics 40 (1), 39–49.
Goodier, J., 1937. On the integration of the thermoelastic equations. Phil. Mag. 7, 1017–1032.
Gordeliy, E., Detournay, E., 2011. A fixed grid algorithm for simulating the propagation of a shallow hydraulic fracture with a fluid lag. Int. J. Numer. Anal. Methods GeoMech. 35 (5), 602–629.
Guo, T., Zhang, Y., Zhang, W., Niu, B., He, J., Chen, M., Yu, Y., Xiao, B., Xu, R., 2022. Numerical simulation of geothermal energy productivity considering the evolution of permeability in various fractures. Appl. Therm. Eng. 201 (Part A), 117756.
Lecampion, B., Desroches, J., 2015. Simultaneous initiation and growth of multiple radial hydraulic fractures from a horizontal wellbore. J. Mech. Phys. Solid. 82, 235–258.
Lecampion, B., Bunger, A., Zhang, X., 2018. Numerical methods for hydraulic fracture propagation: a review of recent trends. J. Nat. Gas Sci. Eng. 49, 66–83.
Lin, R., Peng, S., Zhao, J., Jiang, H., Ren, L., Zhou, B., Wu, J., Song, Y., Shen, C., 2024. Multiple hydraulic fracture propagation simulation in deep shale gas reservoir considering thermal effects. Eng. Fract. Mech. 303, 110147.
Liu, B., Kumar, D., Ghassemi, A., 2025. Modeling proppant transport and settlement in 3D fracture networks in geothermal reservoirs. Geothermics 125, 103176.
Lowell, R., 1976. Comments on 'Theory of heat extraction from fractured hot dry rock' by A. C. Gringarten, P. A. Witherspoon, and yuzo ohnishi. J. Geophys. 81.
Sabha, M., Hofmann, H., Yaghoubi, A., Arjmand, Y., Dusseault, M., 2025. Hydro-shearing and traffic light protocols in mitigating seismic risks: a fully-coupled poroelastic boundary integral modeling approach. J. Rock Mech. Geotech. Eng. 17 (9), 5660–5682.
Tan, P., Pang, H., Zhang, R., Jin, Y., Zhou, Y., Kao, J., Fan, M., 2020. Experimental investigation into hydraulic fracture geometry and proppant migration characteristics for southeastern Sichuan deep shale reservoirs. J. Petrol. Sci. Eng. 184, 106217.
Tan, P., Chen, Z., Fu, S., Zhao, Q., 2023. Experimental investigation on fracture growth for integrated hydraulic fracturing in multiple gas bearing formations. Geoenergy Sci. Eng. 231 (Part A), 212316.
Tang, H., Winterfeld, P.H., Wu, Y., Huang, Z., Di, Y., Pan, Z., Zhang, J., 2016. Integrated simulation of multi-stage hydraulic fracturing in unconventional reservoirs. J. Nat. Gas Sci. Eng. 36 (Part A), 875–892.
Wang, Y., Guo, T., Chen, M., Qu, Z., Hu, Z., Cao, J., Weng, D., 2023. Numerical study on simultaneous propagation of multiple fractures: a method to design nonuniform perforation and in-stage diversion. SPE J. 28 (5), 2514–2533.
Wang, J., Guo, T., Chen, M., Qu, Z., Zhang, B., Zhang, W., Zhai, C., Zheng, P., 2024a. Numerical simulation of fracture propagation morphology in hydraulic fracturing development of geothermal reservoirs based on the CDEM-THM3D. Comput. Geotech. 172, 106444.
Wang, Y., Guo, T., Chen, M., Jia, X., Weng, D., Qu, Z., Hu, Z., Zhang, B., Wang, J., 2024b. Numerical simulation on multi-well fracturing considering multiple thin layers in vertical direction. Int. J. Rock Mech. Min. Sci. 183, 105951.
Wang, Y., Chen, M., Guo, T., Wang, Z., Qu, Z., Zhang, B., 2025a. Propagation of hydraulic fractures and natural fractures: the bypassing behavior in 3D space. SPE J. 30 (1), 65–80.
Wang, Y., Chen, M., Guo, T., Qu, Z., Zhang, B., Lv, M., Wang, W., 2025b. Proppant transport coupled with propagation of three-dimensional hydraulic-natural fractures. Rock Mech. Rock Eng. 58, 2435–2463.
Xia, Y., Yao, M., Li, T., Yang, H., Tang, C., 2024. Numerical analysis of hydraulic fracture propagation in deep shale reservoir with different injection strategies. J. Rock Mech. Geotech. Eng. 16 (9), 3558–3574.
Zhang, B., Guo, T., Qu, Z., Wang, J., Chen, M., Liu, X., 2023. Numerical simulation of fracture propagation and production performance in a fractured geothermal reservoir using a 2D FEM-based THMD coupling model. Energy 273, 127175.

Associate Professor Ming Chen obtained his Master degree from Research Institute of Petroleum Exploration and Development of CNPC in 2016 and his PhD from the China University of Petroleum (Beijing) in 2020. Currently, he is an associate professor in Petroleum Engineering at China University of Petroleum (East China). His research interests mainly focus on the theory of hydraulic fracturing, numerical simulation of hydraulic fracture propagation, fracture diagnostic, and new applications of fracturing in geothermal energy and energy storage.